Nano Energy 89 (2021) 106428

Contents lists available at ScienceDirect

Nano Energy

journal homepage: www.elsevier.com/locate/nanoen

Unraveling the hysteretic behavior at double cations-double halides perovskite - electrode interfaces

Dohyung Kim [a], Yongtao Liu [a,b], Anton V. Ievlev [b], Kate Higgins [a], Olga S. Ovchinnikova [c], Jae Sung Yun [d], Jan Seidel [e], Sergei V. Kalinin [b], Mahshid Ahmadi [a,*]

[a] Joint Institute for Advanced Materials, Department of Materials Science and Engineering, University of Tennessee, Knoxville, TN 37996, USA
[b] The Center for Nanophase Materials Sciences, Oak Ridge National Laboratory, Oak Ridge, TN 37831, USA
[c] Computational Sciences and Engineering Division, Oak Ridge National Laboratory, Oak Ridge, TN 37830, USA
[d] Australian Centre for Advanced Photovoltaics (ACAP), School of Photovoltaic and Renewable and Engineering, University of New South Wales, Sydney, NSW 2052, Australia
[e] School of Materials Science and Engineering, University of New South Wales, NSW 2052, Australia

ARTICLE INFO

Keywords:
Double cations-double halides perovskite
Electrochemical reaction
Interface
Hysteresis
Ion migration
Time-resolved techniques

ABSTRACT

Despite over a decade of research on metal halide perovskites (MHPs) in the context of photovoltaic applications, understanding the nature of electronic and ionic processes associated with current-voltage (*I-V*) hysteretic behavior has been limited. Here, we explore the hysteretic behavior in $(FAPbI_3)_{0.85}(MAPbBr_3)_{0.15}$ perovskite devices with lateral Cr electrodes by applying first order reversal curve (FORC) bias waveform in *I-V*, Kelvin probe force microscopy (KPFM) measurements, and in-situ chemical imaging by time-resolved time-of-flight secondary ion mass spectrometry (tr-ToF-SIMS). In dark, we reveal pronounced hysteretic behaviors of charge dynamics in the off-field by probing time-dependent current and contact potential difference (CPD). Under illumination, transient and hysteretic behaviors are significantly reduced. The tr-ToF-SIMS results reveal that the hysteretic behaviors are strongly associated with accumulation of Br^- ions at the interfaces. In addition, the low mobility MA^+ ions result in transient behavior and contribute to the hysteretic phenomena. It was shown that Pb^{2+} ions can be reduced at the interfaces due to electrochemical reactions with the electrode in the presence of charge injection and photogenerated charges. These hysteretic behaviors associated with charge dynamics, ion migration, and interfacial electrochemical reaction are critical to further improve the performance and stability of MHPs photovoltaics and optoelectronics.

1. Introduction

In recent years, the power conversion efficiency (PCE) of metal halide perovskite (MHP) solar cells have been rapidly improved with PCEs exceeding 25.5% for a single junction solar cell [1]. Beyond photovoltaic applications, the development of these materials for other applications such as light-emitting diode [2], photodetectors [3], ionizing radiation sensors [4] has been remarkable due to their interesting optoelectronic properties. Besides, these materials are now being explored for information technology applications such as memristors [5]. It was recognized that many intriguing properties of MHPs including giant dielectric polarization [6], phase segregation [7], lattice expansion [8], photovoltaic switching [9], anomalous photovoltaic effect [10], and structural variations [11] are inherently linked to ionic behaviors. MHPs are mixed ionic and electronic conductors and the ion migration in these materials generally result from high mobility of ion species especially halides [12–15]. These ionic motions lead to the electrode polarization where the ions with opposite sign to the electrode polarity are accumulated at blocking electrodes [16], or result in electrochemical reactions and charge injections where ions of the same sign as the electrode polarity are generated and injected [11].

In addition to internal electrochemistry of MHPs, the biased electrodes in MHPs can participate in electrochemical processes and ion injections simultaneously [11,17]. Indeed, the metal migration-induced degradation is a critical issue in MHP devices [18]. The common metal electrodes in MHP devices such as Au and Ag can diffuse into the perovskite layer, and result in the escape of volatile species from perovskites [19]. It was observed by us [17] and others [18,20] that not

* Corresponding author.
E-mail address: mahmadi3@utk.edu (M. Ahmadi).

https://doi.org/10.1016/j.nanoen.2021.106428
Received 28 April 2021; Received in revised form 24 June 2021; Accepted 10 August 2021
Available online 12 August 2021

only does the mobile halide ions diffuse into the transport layer, but also either Au or Ag from the electrodes diffuse into the perovskite layer. Besides, the electrochemical reaction between Au and perovskite can lead to degradation of MHP device beginning at the interface. It was shown that the diffused Au ions at the interface interact with halide ions forming gold halide complexes under illumination condition [17]. This is consistent with a recent article noting that MHP stability relies on the interfacial conditions [21,22]. To address this issue in MHP solar cells, several strategies have been proposed including designing barrier layers [19] such as Cr interlayer as diffusion barriers [18], modification of hole transport layer with Al_2O_3 nanoparticles [23], and device processing at elevated temperature [18]. It has been revealed that Cr layers can be used to stabilize the interface of perovskite solar cells [24,25] and reduce interfacial recombination [26]. The work function of Cr electrode is ~4.37 eV, which is similar to the work function of Ag, ~4.26 eV. Considering the conduction band and valance band energy of perovskite, the work function of Cr allows for efficient carrier extractions. It should be note that ultimately, commercializing perovskite solar cells requires the use of cheap electrode materials such as Cr [24,27,28], Cu [28,29], and carbon [24]. Thus, a more insightful understanding of electron/hole and ion transport at electrode interface is critical to further improve the stability of photo-current and -voltage output of MHP-based devices.

Necessity to understand the behavior of MHPs in the device setting has stimulated a broad number of studies targeting the time-dependent charge dynamics, preponderantly based on variants of Kelvin probe force microscopy (KPFM) [30–33]. Previous study via KPFM confirmed that the macroscopic current-voltage (*I-V*) hysteresis behavior could be associated with trapped charges and ion migration across perovskite layer [34]. High speed-KPFM offered mapping local changes in the open-circuit voltage (V_{oc}), revealing nanoscale voltage domains with ~ 16 s frame rate [32]. Recently, the development of G-mode KPFM [35,36] allowed us to identify contact potential difference (CPD) with μs time scale resolution, revealing the fast response dynamics in MHP film [31] and single crystal devices [37]. Further, ionic and electronic charge transports were mapped using time-resolved (tr)-KPFM technique [38] with ms time scale resolution in a lateral Au/CH_3NH_3(MA)PbI_3/Au device, resulting in different CPD distribution due to chemical gradient induced by application of external electric field [30]. In general, CPD changes in KPFM measurements can be associated to the surface photovoltage, surface charging, and electronic/ionic charge transport behaviors [39].

Recently, we used time-resolved time-of-flight secondary ion mass spectrometry (tr-ToF-SIMS) to demonstrate the time evolution of ion distribution in $MAPbI_3$ films, revealing hysteretic behavior in MA^+ and I^- motions [40]. This result is correlated with a remanent current, especially under illumination, which also contributed to the hysteretic behavior [40]. It was revealed that MA^+ migration is more dominant than halide (I^- or Br^-) migration in $MAPbX_3$ (X = I, Br) films using tr-ToF-SIMS [41]. Nonetheless, the nature of electronic and ionic processes remains fully understood yet. This is especially the case for double-cations and double-halides perovskites that have attracted much attention due to high efficiencies [42–44] and remarkable long-term stability of solar cells based on these compositions [45–47]. Due to the presence of multiple mobile cations and anions, these compositions are expected to demonstrate more complex interplay between electronic and ionic processes. Thus, a combination of multiple techniques with different strengths is necessitated to provide a better understanding of the electronic and ionic processes in double-cations and double-halides perovskites.

In this study, we explore the interfacial and bulk electrochemical dynamics in Cr/$(FAPbI_3)_{0.85}(MAPbBr_3)_{0.15}$/Cr lateral devices using the combination of time- and voltage-dependent *I-V*, KPFM, and tr-ToF-SIMS measurements. This integrated approach allows identification of both spatial localization and nature of the involved species, establishing the interplay of electronic and ionic dynamics in these systems. To study the time dynamics, we use a bias waveform referred as a first-order reversal curve (FORC) that allows separating bias-induced chemical effects. Originally, FORC method has been introduced for probing distribution of switching fields in classical ferromagnetic [48] or ferroelectric materials [49]. Recently, FORC approach was extensively applied in the tip-based *I-V* measurements [50–53], piezoresponse force microscopy (PFM) [49,54,55] and electrochemical strain microscopy (ESM) [52,53,56]. Here, we extend this approach to *I-V*, KPFM, and ToF-SIMS measurements. A gradually increasing and decreasing pulsed bias is applied stepwise with on- and off-field waveform to the lateral Cr/$(FAPbI_3)_{0.85}(MAPbBr_3)_{0.15}$/Cr device to simultaneously inject and release electronic and ionic charge species. The FORC *I-V* measurement with on- and off-field pulses is performed to characterize the current behavior in dark and under illumination in the devices. The FORC waveform is also applied to the KPFM measurements to explore spatial- and time-resolved CPD distribution in the devices. Moreover, using an in-house tr-ToF-SIMS, the time-dependent ionic distribution is explored upon application of on- and off-field biases in dark and under illumination. The distribution of negative (I^-, Br^-) and positive (MA^+, FA^+) ions in on- and off-field biases is analyzed using a non-negative matrix factorization (NMF) method to efficiently separate the information from multiple peaks at once. Our results clearly reveal the time- and voltage-dependent charge dynamics and nature of mobile ion species in double-cations and double-halides perovskite and elucidate the origin of hysteresis in the lateral devices.

2. Results & discussions

Lateral Cr electrodes with channel distance of around 70 μm and 50 nm thickness were deposited by thermal evaporation on solution-processed 300 nm thick double-cations and double-halides perovskite $(FAPbI_3)_{0.85}(MAPbBr_3)_{0.15}$ thin films on glass substrates [30,40]. Details of fabrication procedure is described in the experimental section. X-ray diffraction was performed to confirm the structure of as-synthesized perovskite film (Fig. S1). The XRD patterns correspond to the planes of $(FAPbI_3)_{0.85}(MAPbBr_3)_{0.15}$ which is similar to previous studies [11,42,57].

First, to explore the ionic behavior in the $(FAPbI_3)_{0.85}(MAPbBr_3)_{0.15}$ perovskite devices, we have systematically investigated the time- and voltage-dependent transport properties. Here, we utilize the time-delayed FORC method as shown in Fig. 1a, adapted from waveforms previously used in dynamic-PFM [49,54,55,58] and ESM [52,53,56]. Note that a series of bias pulses with a given magnitude followed by a zero-bias in each step are applied to the system and the evolution of current is measured as a function of time during both on- and off-fields. For the materials with purely resistive or non-linear behavior, the response will be a simple ohmic current independent of time. In the presence of linear capacitive phenomena, the current will be an exponential function of time with the time constant dependent on the RC time constant of the system. Finally, in the presence of the ionic and electrochemical phenomena, the time dependence of currents in the on- and off-field will be determined by the electrochemical phenomena at the interfaces. Importantly, the sign of the current allows clear differentiation of the electrode polarization from charge injection.

Here, we investigate charge dynamics via time dependence of current behavior. Fig. 1a shows a schematic illustration of the experimental set-up for *I-V* and KPFM measurements induced by a FORC bias waveform with on- and off-fields in dark and under illumination. All experiments are carried out under ambient and low humidity (< 20%) conditions. The KPFM results are consistent over several repetitive measurements under low humidity conditions. In fact, water penetration under high humidity (> 50%) conditions occurs at grain boundaries, which causes a significant increase of ion migration, accompanying topological changes [59]. During our experiment, we do not observe such changes on the film surface as shown in Fig. S2. Note that in the waveform the on-field is set when the bias is consecutively on from 0 to

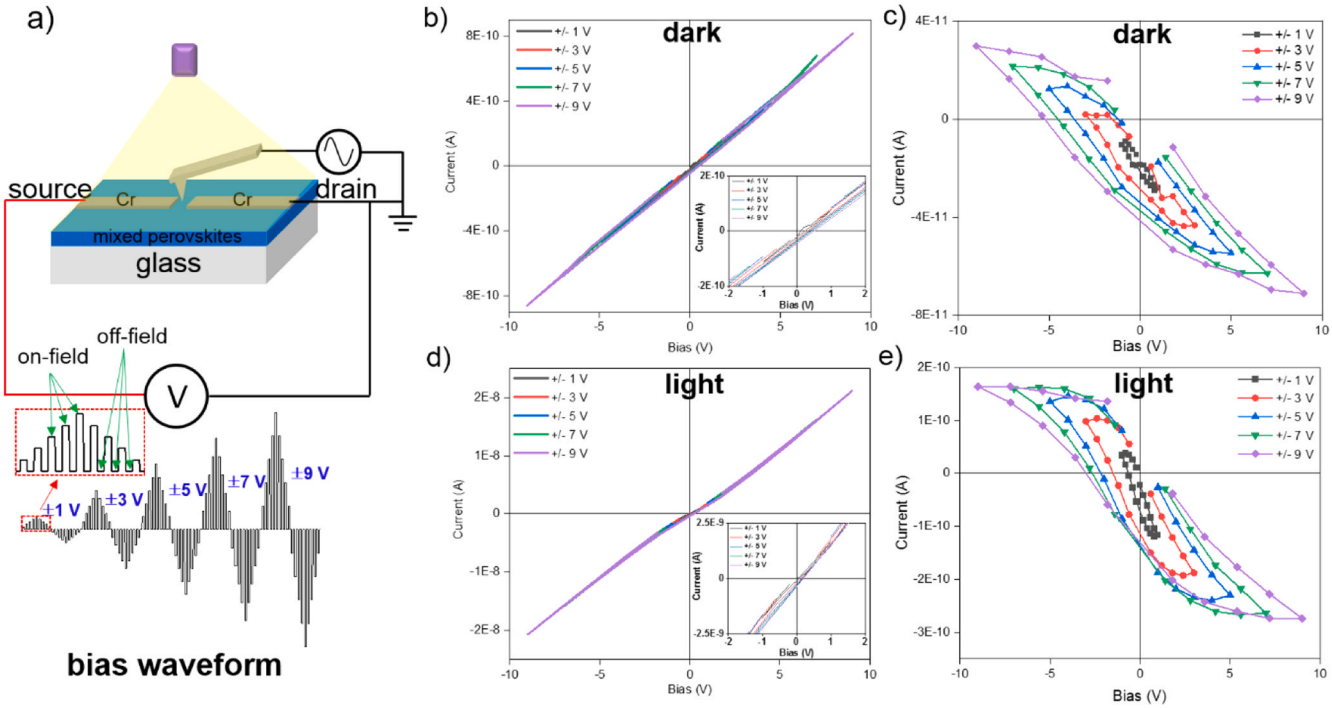

Fig. 1. FORC bias with on- and off-field driven *I-V* characteristics of the lateral perovskite device in dark and under illumination. (a) Schematic illustration of the experimental set-up and the FORC bias waveform applied on the lateral device (top). The corresponding stepwise waveform evolves in 9 steps at each bias (bottom). (b) *I-V* characteristics when biases are applied (on-field) and (c) when the bias is turned off after the on-field (off-field) in dark and (d,e) under illumination.

+ 1, − 1, + 3, − 3, + 5, − 5, + 7, − 7, + 9 and − 9 V at a regular interval of 21.56 s with shape following a triangular envelope, and the off-field is set during bias-off steps after each bias-on pulse, resembling typical hysteresis loop measurements [60]. Detail explanation of FORC bias waveform can be found in Supplementary Note 1. During video recording of the device under an optical microscope, we do not observe the appearance of any color change due to degradationat the electrode or perovskite regions while applying bias waveforms. Fig. S3 displays the captured images of the device during FORC *I-V* measurements. Upon the application of electric biases, the device current gradually increases and decreases in the range between 0 to ± 1.0 nA as shown in the current-time (*I-t*) response in Fig. S4a. In each step, as soon as a voltage is applied, we observe a sharp increase in the current followed by a current decay (Fig. S4). Similar current transient behavior was previously observed for lateral Au/$MAPbI_3$/Au devices with a decay time in the range of tens to hundreds of ms until a stable state reached [40]. However, here the current decay shows an exponential decay reaching a stable state after hundred ms to a few seconds, suggesting the existence of a slower mechanism (Fig. S4c). In addition, the *I-t* response shows sharp current spikes with opposite directions during off-fields. This sharp current spikes possibly originate from the capacitive effect [61] which has a faster dynamics than ion migration under electric bias and illumination condition. The capacitive effect in Cr/$(FAPbI_3)_{0.85}$($MAPbBr_3)_{0.15}$/Cr device is much slower than our previous study using Au/$MAPbI_3$/Au device possibly due to the slower ion dynamics in the double cations and double halides perovskite and the small difference between the dielectric constant of the materials. Similarly, we perform FORC-driven *I-V* measurements on a Au/$(FAPbI_3)_{0.85}(MAPbBr_3)_{0.15}$/Au device (see Fig. S5). We note that the current in the Au device is one order of magnitude lower than the Cr device especially at larger biases. By fitting the current decay at + 9 V, the decay is slightly faster in the lateral Au device. The small difference might be due to higher resistance of Cr electrode than Au, which can cause higher capacitive effect with slow decay. We note that the current cannot fully stabilizes during the off-field condition and such behavior becomes more significant at higher biases (Fig. S4a). This behavior could be due to ion migration as ions are expected to actively migrate under larger biases [11,34]. To avoid capacitive effect in dark condition, the on- and off-field currents are extracted from nearly stabilized currents at each voltage, as can be seen in Fig. 1b,c for all bias steps. The extracted currents at each bias step in the on-field loops are shown in Fig. 1b and the inset demonstrates linear and sharp shaped current dynamics with small hysteretic behavior as a function of bias. This is due to the contributions from an electrostatic effect accompanying electronic charge injection at the electrodes and the hysteretic behavior might be induced by ion migration. In our previous study, we directly mapped charge injection near the interface of lateral $MAPbBr_3$ single crystal device in dark condition [11]. Meanwhile, the off-field loops (Fig. 1c) show banana-shaped hysteretic behavior, potentially resulting from ion redistribution. These behaviors clearly reveal that hysteresis loop opening starts at relatively small biases (±1 V), indicating the onset of ion relaxation and redistribution at these minute voltages. To investigate the behavior of charge transport under illumination, FORC *I-V* measurements are carried out under a white LED source. Upon application of electric bias (on-field), the photocurrent gradually increases and decreases between 0 to ±20 nA. As can be seen in Fig. S6, the *I-t* response exhibits less transient behavior as compared to dark condition due to high density of photogenerated charges. We can also clearly see the photocurrent effect between on- and off-field conditions in Fig. 1d,e. We observe the electrostatically linear dynamics with small opening loops in the on-field currents in Fig. 1d. These behaviors are relatively similar to the dark condition with the exception of slightly non-linear *I-V* behavior. This dynamic can be associated with interfacial trap-filling [62] or interfacial resistance induced by Cr contacts [26] due to large density of photogenerated carriers. It is interesting to note that the off-field currents (Fig. 1e) are narrow with sharp-edged hysteresis loops. This behavior will be further explored using KPFM technique. We clearly note that the hysteretic *I-V* behaviors in the off-fields are particularly different between dark and under illumination conditions.

To gain further insight into the spatial localization of the electronic

and ionic charges, we use the same FORC bias waveform during KPFM measurements. The measurements are carried out between source to drain electrodes across perovskite channel regions. The details are described in the experimental section. Fig. 2a,b show the topography image and initial CPD spatial map before applying any bias, clearly identifying the source, perovskite, and drain regions with different surface potential maps. Using KPFM, we can typically map the local surface potentials caused by ions, static and dynamic electric potentials, electric fields, and charge carrier distribution [11,39,63]. Once a voltage is applied to the source electrode, the KPFM results in different CPD distribution at each region corresponding to the bias profile as a function of time. The CPD maps at different regions of device in dark condition are shown in Fig. S7a–c. The CPD is dependent on varying biases as expected. The CPD spatial maps of device under illumination are displayed in Fig. S8a–c. Note that the KPFM images under illumination are taken on the same topography used in dark condition with 40 min relaxation time after the measurements in dark to ensure the device returns to the initial CPD. This also confirms no visible degradation in the topography after the measurement in dark condition. Similarly, the CPD under illumination is dependent on the applied bias. Notably, no degradation was observed even after the measurement under illumination.

The on-field CPD distribution extracted from CPD maps in dark is plotted in Fig. S9a scanning from source to drain regions where potentials correspond to the applied bias. During biasing, the detected surface potential in dark condition was found to increase and decrease relatively linearly in the perovskite region while potential drops are observed at both electrode interfaces (Fig. S9a). The potential drop at the interface between source and perovskite indicates an accumulation of negatively or positively charged species, suggesting all injected charges are from the source electrode. Besides, the on-field CPD distribution between forward- and reverse-biased device is relatively symmetric. The change in CPD in the on-field condition agrees with our previous study [11] when applying positive and negative biases to the lateral Au/MAPbBr$_3$/Au single crystal device results in a symmetric surface potential change. However, in the off-field conditions as shown in Fig. S9b, the CPD line profiles from the source to drain electrodes significantly change as a function of bias. We speculate that the either electronic charges or ions do not immediately return to the initial state within 22 s scan time, corresponding to the off-field *I-V* characteristic in Fig. 1c. This is because gradually increasing electrical biases cause longer time for charge carriers to relax and ions to redistribute and hence this induces a remnant field after bias removal. Consequently, the density of accumulated charges at the interface slightly changes depending on the bias step. Under illumination, CPD distributions between source and drain electrodes at all on-field steps are shown in Fig. S10a. The result reveals that CPD linearly increases and decreases as a function of bias across source to drain electrodes with similar potential drops at each interface. Note that there are higher potential drops at source-perovskite interface under illumination compared to the dark condition. Interestingly, we observe potential drops at both interfaces from CPD distribution in off-field condition (Fig. S10b). The observed potential drops are significant at larger biases (above ±5 V) than smaller biases (below ±3 V). Particularly, higher potential drops are observed at source-perovskite interface at positive biases, + 5, + 7, + 9 V while higher potential drops occur at drain-perovskite interface at negative biases − 5, − 7, − 9 V. This indicates more accumulated charge carriers near these interfaces compare to the dark condition. Basically, the accumulation of charge carriers at the interface is due to the drift of both electronic and ionic charges to the opposite electrodes, which can influence on the hysteresis phenomenon. It takes longer time for the accumulated charges at the interface in the off-field condition to relax.

To explore time-dependence of CPD variation at individual regions in dark, e.g., source-perovskite interface, perovskite, and perovskite-drain interface, *CPD-t* curves were extracted from each region of CPD maps (shown in Fig. S11). As expected, the CPD at source-perovskite interface

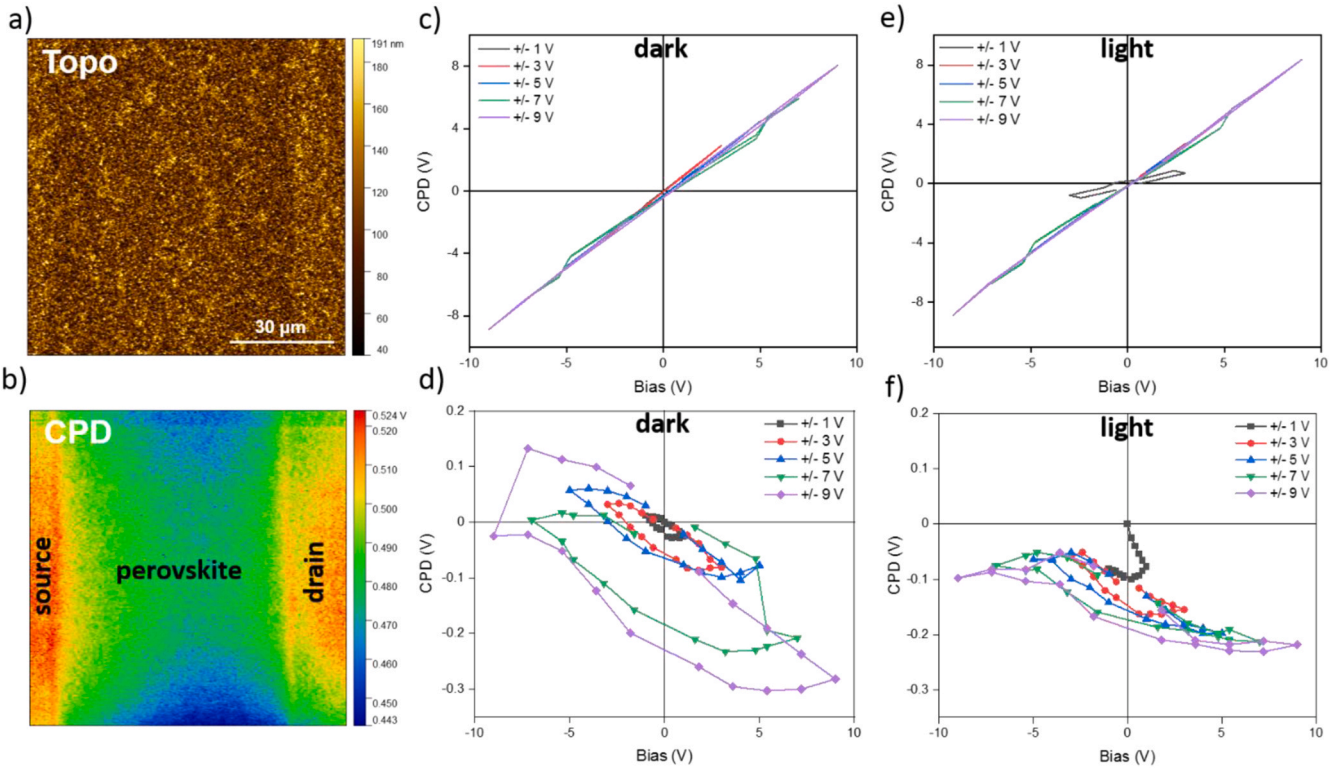

Fig. 2. FORC bias with on- and off-field driven KPFM measurements in the lateral perovskite device in dark and under illumination conditions. (a) Topography image of lateral perovskite device over an area of 90 μm^2 in dark. (b) CPD spatial map, indicating source, perovskite and drain regions. (c) Average CPD plot at the interface between source electrode and perovskite extracted from each bias step during on-field and (d) off-field in dark condition and (e,f) under illumination.

(Fig. S11a) varies significantly while the change at the perovskite-drain region is negligible (Fig. S11c). The changes in CPD at the perovskite region can be seen in Fig. S11b. Interestingly, we notice negative CPDs in the off-field conditions for positive biases and vice versa in all three regions associated with charge relaxation (see the enlarged CPD in Fig. S11d–f). To discern this phenomenon, we separated the CPD distributions in on- and off-fields. Fig. 2c,d shows average CPD at each bias step in on-field conditions at the source-perovskite interface. The average CPD plots in other regions, e.g., perovskite region, and perovskite-drain interface are shown in Fig. S12. Similar to the *I-V* characteristics, the CPD variations in on-field (Fig. 2c and Fig. S12a, c) show linear behavior with small open loops at all regions. These open loops are related to accumulation of electronic and ionic charge species, especially at higher biases where ions are likely to drift faster. However, in the off-field conditions (Fig. 2d and Fig. S12b, d), nonlinear potential variations are observed, and more hysteretic behaviors can be seen at the interfaces compared to the bulk perovskite region. The range of changes in CPD is around 300 and 200 mV at ±9 V at the source-perovskite interface and the perovskite-drain interface, respectively. However, the CPD variation is smaller at the perovskite region (around 150 mV at ±9 V). The significant potential variation at the interface indicates higher density of accumulated charge carriers and ions. We note that the accumulation of negatively or positively charged species at each interface under forward- and reverse-biases can lead to hysteresis in the potential variations during off-field conditions.

We further investigate the evolution of time-dependent potential variations in the vicinity of the interfaces of source-perovskite, perovskite-drain electrodes, and bulk perovskite under illumination. As can be seen in Fig. S13, both transient effect during on-fields and CPD variation in the off-field conditions are significantly decreased as compared to the *CPD-t* curves in dark condition (Fig. S11). Here, we study the individual potential responses in the on- and off-fields at the source-perovskite interface as shown in Fig. 2e,f. During the on-field condition (Fig. 2e), the CPD variations are generally linear except for a visible loop at ±1 V which is due to photogenerated charge carriers. However, in the off-field, the hysteresis loops are significant in all biases (Fig. 2f). Such loops are similar to the hysteretic loops in the *I-V* curves (Fig. 1e). The average CPD plots at the perovskite region and perovskite-drain interface in the on- and off-fields are displayed in Fig. S14. Clearly, the hysteresis behavior in CPD during the off-field conditions is significantly reduced at perovskite region and perovskite-drain interface than in perovskite-source interface. Compared to dark condition, the reduced transient behavior under illumination originates from faster charge dynamics (ms to μs time scale) due to higher density of photogenerated charge carriers. Previous studies showed that light induces fast charge dynamics in MHPs using electrochemical impedance spectroscopy [64–66,102]. The fast and slow dynamics in MHPs have a common origin associated with a charge distribution. Consequently, the extent of hysteretic and transient behaviors in the *I-V* and KPFM results clarify that a fast charge dynamic is dominant under illumination.

It has been theoretically demonstrated that the charge traps that act as recombination sites strongly interact with ions as well as electronic charge carriers [67]. The extent of the trapping charge carriers is dependent on bias-induced ion distribution [67]. Further, it was computed using a numerical device modeling that ion accumulation derives from both interfacial recombination and injected charge carriers from the source electrode [68]. Thus, the role of ion migration is critical due to higher non-radiative recombination rate at the interface as it can potentially lead to higher hysteretic behavior at the interface. The application of bias to the lateral electrode device, may initiate several processes such as spontaneous polarization, electrochemical polarization at the interface owing to surface charge motions, and electronic and ionic charge injection from biased electrodes [69]. Typically, the applied biases to the electrodes cause charge injection, resulting in positive and negative surface potentials in the KPFM maps as the injected electronic or ionic charge carriers can move to the opposite electrodes. Likewise, our KPFM results show positive or negative surface potentials when a bias is applied to the electrodes. Besides, the CPD difference between the detected surface potentials in the perovskite bulk and at the interface with electrodes is larger as the bias increases. This potential difference is directly related to the density of charge injection from the biased electrodes. Herein, the charge carriers near interfaces include electronic charge carriers injected from external circuit and the ionic charge carriers induced from electrochemical reaction between the perovskite and electrodes. This manifests laterally applied electric field between the electrodes does not lead to spontaneous polarization but to the injection and relaxation or redistribution of charges. Here, we study the polarization effect of electronic and ionic charge carriers on the double-cations and double-halides perovskite surface using time- and bias-dependent KPFM. FORC driven KPFM measurements in the time domain provide an insight to the mechanisms of charge nature, injection, relaxation and their motions via the temporal evolution of the electric potentials and CPD variations.

Although many mixed perovskite devices suffer from phase segregation, this phenomenon occurs severely in compositions with higher Br [70] concentration, especially above 25%. This was attributed to the strain activated light-induced phase segregation in mixed perovskites with higher Br concentration [70]. It was recently reported that type and concentration of organic cations can be also responsible for phase segregation in mixed perovskites [71]. We previously studied the phase segregation in the $(FAPbI_3)_{0.85}(MAPbBr_3)_{0.15}$ composition using photoluminescence (PL) spectroscopy, revealing no peak splitting over time under illumination [11]. This result suggests that phase segregation does not occur in this composition under similar experimental conditions. As mentioned, the phase segregation in mixed perovskite is strongly related to the concentration of halide ions, especially Br concentration. Although several studies [71–75] show the light-induced halide segregation in the mixed perovskites, these studies are performed on compositions with higher Br concentration, e.g., 30% or 50%. In fact, the solar cells using $(FAPbI_3)_{0.85}(MAPbBr_3)_{0.15}$ composition showed highly efficient and stable performance [11,34,76,77]. Further, it has been recently demonstrated that light-induced halide segregation is absent in $MAPb(I_{0.85}Br_{0.15})$ perovskite due to suppression of local strains while the phase segregation from localized strains occurs as Br concentration increases [70]. It should be noted that we also use a very weak light with an intensity between 0.1 and 0.3 mW cm^{-2} in our measurements, and therefore we do not expect serious phase segregation during illumination.

It is commonly believed that a higher ion migration could be strongly associated with defect densities in MHP films [78–80]. To confirm this, we explore morphological defects in different compositions of MHPs using KPFM measurements (Fig. S15). As can be seen in Fig. S15, the dark regions with small CPD in the films are composition dependent. Using local PL imaging integrated with SEM microscopy, it was shown that the dark regions have greater nonradiative recombination loss [81]. Recently, dark regions with small CPD are explored by Stranks et al. [82], revealing nanoscale trap clusters due to local excess of halide ions in the mixed perovskites. As can be seen in Fig. S15b,c, these clustered traps significantly increases when $MAPbBr_3$ concentrations is above 30% while the $(FAPbI_3)_{0.85}(MAPbBr_3)_{0.15}$ composition has the lowest concentrations of defects. This result suggests that the composition of mixed perovskites can affect the hysteretic behaviors.

To explore the evolution of ionic distribution and electrochemical dynamics on the lateral device, time-dependent ion dynamics are measured using an in-house custom built tr-ToF-SIMS technique (Fig. 3a). In these measurements, a similar bias waveform was applied during the measurements with 9 s time steps, and the ToF-SIMS results was acquired across the electrodes. Our results reveal the dependence of ions distribution to the applied electric biases and time. This measurement allows us to directly observe the temporal evolution of ions mass transfer, ions relaxation and redistribution during on- and off-field conditions. Fig. 3b shows the average mass spectra of negative ions

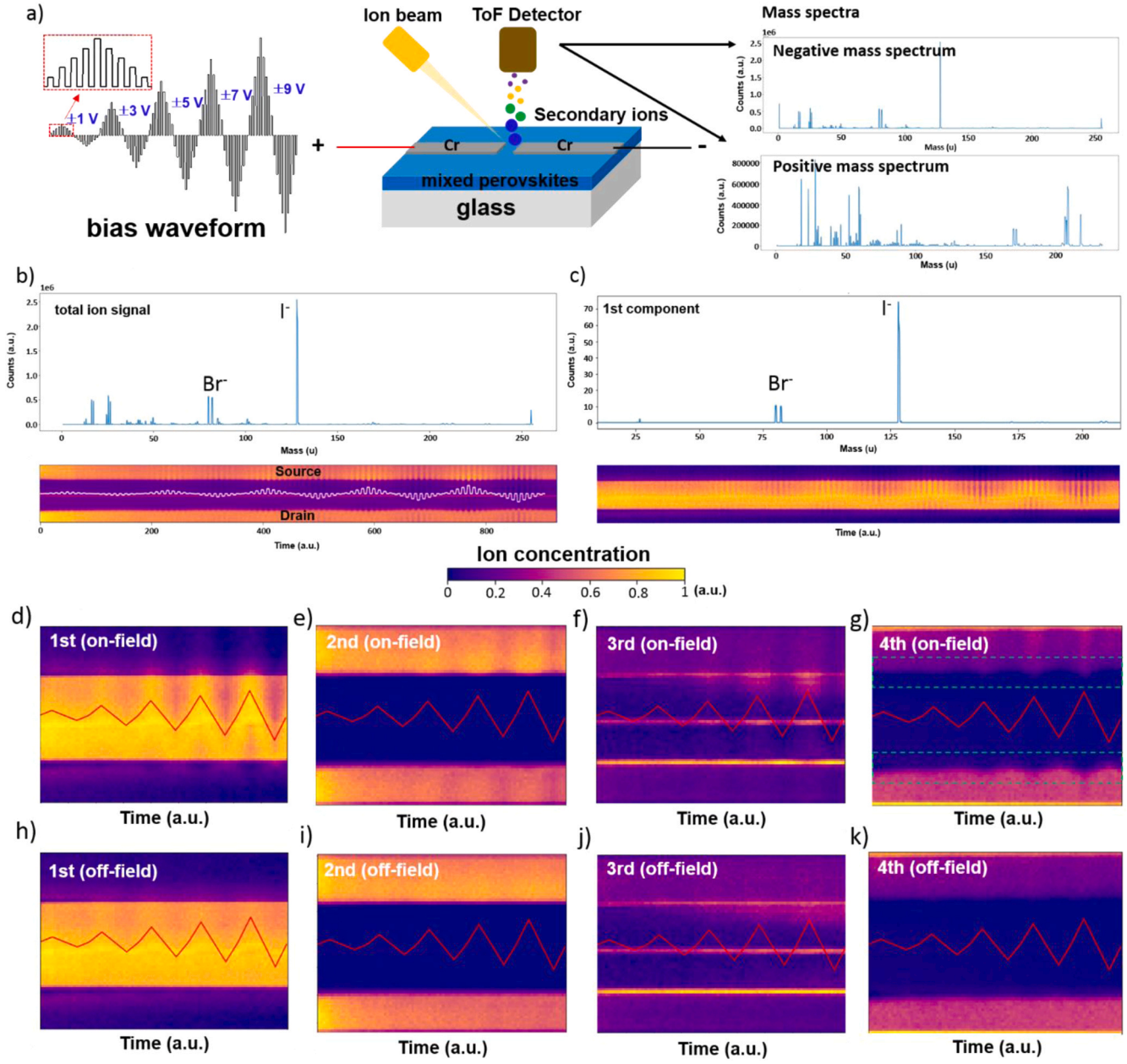

Fig. 3. The temporal evolution of negative ions in operando measured by tr-ToF-SIMS in the lateral perovskite device in dark condition. (a) A schematic illustration of tr-ToF-SIMS driven with FORC bias waveform during on- and off-fields. (b) The total mass spectra of negative ions (top) and the corresponding tr-ToF-SIMS map as a function of time and bias waveform (bottom). (c) The 1st NMF decomposition of tr-ToF-SIMS results (top) and the corresponding loading map as a function of time and bias (bottom). (d) The 1st, (e) 2nd, (f) 3rd, and (g) 4th NMF components of tr-ToF-SIMS maps in the on-field condition, and the (h) 1st, (i) 2nd, (j) 3rd, and (k) 4th NMF components in the off-field for negative ions in dark condition.

accompanied with the time- and voltage-dependent map of all negative ion distribution. Particularly, halide ions, e.g. I^- and Br^-, are highly concentrated in this spectrum. Note that the top and bottom areas refer to the source and drain electrodes, respectively.

To map the time- and voltage-dependent ionic dynamics in the multidimensional ToF-SIMS data sets (Fig. 3b), we utilize an unsupervised machine learning analysis method, non-negative matrix factorization (NMF) to reduce the dimensionality of the data sets allowing for natural and physical constraints present in the system. This method allows us to analyze unmixing components and find sparse features from a total ion signal. NMF is chosen as the simplest method that yields non-negative components. More details of this analysis method can be found in Supplementary Note 2 and our previous study [17]. The ToF-SIMS data is represented as a linear combination of non-negative components in the equation below:

$$X_i = \sum_j v_i v_j + N_i$$

In NMF, ions distribution profile X_i is unmixed on weigh coefficients v_ia linear combination of endmembers v_j (N_i, noise) subject to $v_i \geq 0$. Using NMF, the total response of negative ions mass spectra (Fig. 3b) is decomposed into 4 components that are optimized to elucidate the spatial distribution of different ions. The 1st NMF component (Fig. 3c) shows time-and bias-dependence of negative ions distribution (I^- and Br^-). As can be seen, a relatively higher intensity of I^- ions mass is counted as compare to the Br^- ions due to the higher concentration of I^- in $(FAPbI_3)_{0.85}(MAPbBr_3)_{0.15}$ stoichiometry. Other 3 NMF components are displayed in Fig. S16. The 2nd NMF component (Fig. S16a) also

shows relatively higher intensity of I^- ions in addition to small concentration of organic molecules such as CH^-, CN^-, etc. particularly at the electrode regions. The presence of these organic molecules possibly results from bias-induced dissociation of MA^+ in the perovskites. Meanwhile, the 3rd NMF component shows the accumulation of Br^- and I^- ions at the source and drain interfaces and center regions (Fig. S16b). We speculate that the detected ions at the center region could be possibly due to attraction of Na^+ ions placed at central area (This will be discussed in next section). Comparably, Br^- ions are more dominant at the drain interface. This result elucidates that the Br^- ions are more mobile and especially accumulated at the perovskite-drain interface during the application of bias waveform. Most recently, a distinct depletion of Br^- ions at one interface and irreversible accumulation of them at the opposite interface were experimentally shown after operating under light and bias in a triple cation $(Cs_{0.06}FA_{0.79}MA_{0.15})Pb(I_{0.85}Br_{0.15})_3$ perovskite device. It was explained that the depletion and accumulation of Br^- ions at the interface creates barriers for charge transport and increases nonradiative recombination. The observed accumulation of Br^- ions in our result is in good agreement with the aforementioned study. These accumulated ions at the interface could be associated with the observed potential drops in the CPD distribution. Here, interfacial ion accumulation is mostly associated with Br^- ions. Understanding the ionic behavior at the interface is critically important as this phenomenon plays a crucial role in determining the device stability and performance such as modulation of carrier transport barriers, built-in electric field, charge accumulation and extraction. Finally, the 4th NMF component, shown in Fig. S16c contains hydrocarbons on the Cr electrode surface, similar hydrocarbons were previously observed on the Au electrode in lateral $MAPbBr_3$ single crystal devices possibly due to the formation of organic impurities, byproducts and volatile species during synthesis and characterization.

To further explore the chemical changes during the on- and off-field conditions, we separate the maps of on-field and off-fields components of NMF analysis carried out on the full dataset (Fig. 3d–k). Interestingly, transient behaviors are observed in all NMF components during the on-field condition (Fig. 3d–g). Particularly, in the 3rd NMF component during on-field (Fig. 3f), halide ions are higher concentration at the source interface when applied positive biases. This directly indicates that halide ions migrate towards the source interface at positive bias and they migrate to the drain interface at negative bias during on-field. This migration is also observed in central region. In the 4th NMF component during on-field (Fig. 3g), we observe significant migration of small molecular ions (see Fig. S16c) at the interface. This result implies that the ions with lighter masses, e.g., organic molecules are interacted with the electrodes during on-field condition. Further, during off-field conditions, halide ions are relaxed in the bulk region (Fig. 3h–k), while the accumulation of halide ions is still observed at the interface regions in the off-field condition (Fig. 3j). This demonstrates that halide ions almost relax in off-fields which takes 9 s. It is worth to note that the accumulation of halide ions at the interface in the 3rd NMF component in the off- field (Fig. 3j) is a direct evidence of the effect of ions on the charge transport. The hysteresis behavior in the *I-V* and *CPD-V* during off-fields can be attributed to the accumulation of halides at the interface.

The ions distribution is further explored via tr-ToF-SIMS where a built-in white LED placed inside the chamber for illumination. The temporal evolution of ions upon application of electric bias is shown in negative mode (Fig. S17a). Likewise, the total mass spectra are decomposed into the 4 NMF components (Fig. S17b–e). Here, the NMF loading maps reveal less transient behavior in the ion distribution compared to the dark condition. This less transient behavior was also observed in the *I-V* and CPD results. Under illumination, the less transient behavior, and especially higher conductivity in the *I-V* curve are associated with light-induced ultrafast ion migration [83,84], as well as higher concentration of fast photogenerated charges. The separated NMF maps in the on- and off-fields are also shown in Fig. S18. Similar to the dark condition, accumulation of halide ions, especially higher concentration of Br^- ions at the interface is observed in the 3rd NMF component of mass spectra under illumination. The accumulated Br^- ions at the interface can have both detrimental effect on charge transport [85] and beneficial effect as increased concentration of Br^- ions at the interface between perovskite and transport layer has shown to enhance electron extraction [86]. This was attributed to the fact that the accumulated Br^- ions play a critical role in passivating defect states at grain boundaries and interfaces in MHPs [86]. Thus, controversy remains regarding the effect of the accumulated Br^- ions at the interface. Nonetheless, our result provides direct visualization of the accumulated Br^- ions at the interface of $(FAPbI_3)_{0.85}(MAPbBr_3)_{0.15}$ as a function of electric bias both in dark and under illumination.

To compare ion dynamics and interfacial effect, we also perform tr-ToF-SIMs on Au/$(FAPbI_3)_{0.85}(MAPbBr_3)_{0.15}$/Au device. We observe the traces of Au ions diffused at the interface and over the perovskite region especially under illumination (Fig. S19d,e). We further analyze the spatial distribution of mass spectra in distinct regions including the Au electrode, interface, and perovskite, as shown in Fig. S19a–c. The spectrum of Au ions mass is clearly observed at the interface and perovskite regions. Besides, the traces of I^- ions are observed in the Au electrode region both in dark and under illumination (Fig. S19f,g) during the application of FORC bias. We also detect I^- ions in the Au electrode region in the mass spectra (Fig. S19a) while no Br^- ions can be detected in the electrode region from the ToF-SIMS chemical maps (Fig. S19h,i). This result suggests that I^- ions can migrate to the Au electrodes during operation conditions. However, Br^- ions accumulate at the interface area (Fig. S19h,i). The mass spectrum in Fig. S19b confirms high concentration of Br^- ions at interface than in the Au electrode (Fig. S19a). The diffused Au ions at the interface and further into the perovskite regions, and formation of gold halide complexes can ultimately lead to the degradation of MHP-based devices.

To explore the changes in positive ions behavior in operando, the mass spectrometry is performed in positive mode. Fig. 4a shows the average mass spectra of positive ions and the corresponding chemical map as a function of time and bias waveform across the electrodes. Likewise, using NMF analysis, the total response of positive mass spectra in operando was decomposed into the 4 NMF components. The 1st NMF component in Fig. 4b shows the presence of positive ions such as FA^+, MA^+, Pb^{2+}, Cr^+ and Na^+ ions where Na^+ ions are possibly migrated from the glass substrate [87]. The other NMF component maps are exhibited in Fig. S20. Interestingly, we found that there is a central line at the bulk region in the 2nd NMF map in Fig. S20a and the corresponding mass spectra show the contribution from Na^+ and FA^+ ions. This line can be also seen as a depleted region in Fig. 4b. Na^+ ions can already diffuse into the perovskite layer during thermal annealing of perovskite films and its storage in a N_2-filled glove box [87]. To investigate the migration of Na^+ ions, we prepared perovskite films on a different glass substrate with lower quality (AmScope, BS-72P) and performed ToF-SIMS on the device. As shown in Fig. S21a, a higher concentration of Na^+ ions were detected at the bulk region between the electrodes. The results further show that after forward- and reverse-biasing the electrode, the observed Na^+ ions migrate towards both biased electrodes as shown in Fig. S21b. It was previously shown that a large density of Na^+ ions can move from the glass substrate along the perovskite grain boundaries and passivate defects [87]. The coupling between Na^+ ions and defect sites in MHPs is also reported [88]. The Na^+ ions can move to the interstitial sites or fill the MA vacancies, resulting in improvement of structural stability in perovskites [88]. Similarly, Na migration was observed in encapsulated polycrystalline silicon modules leading to potential degradation in these modules due to generating shunted areas [89]. The Na ion migration from a soda lime glass could lead to either beneficial or detrimental effects and become a general phenomenon in photovoltaic devices.

Although the observed central line in the ion distribution map is mainly contributed by Na^+ ions, there is a minor effect by FA^+ ions (Fig. S20a). Next, the 3rd NMF component (Fig. S20b) indicates the Cr

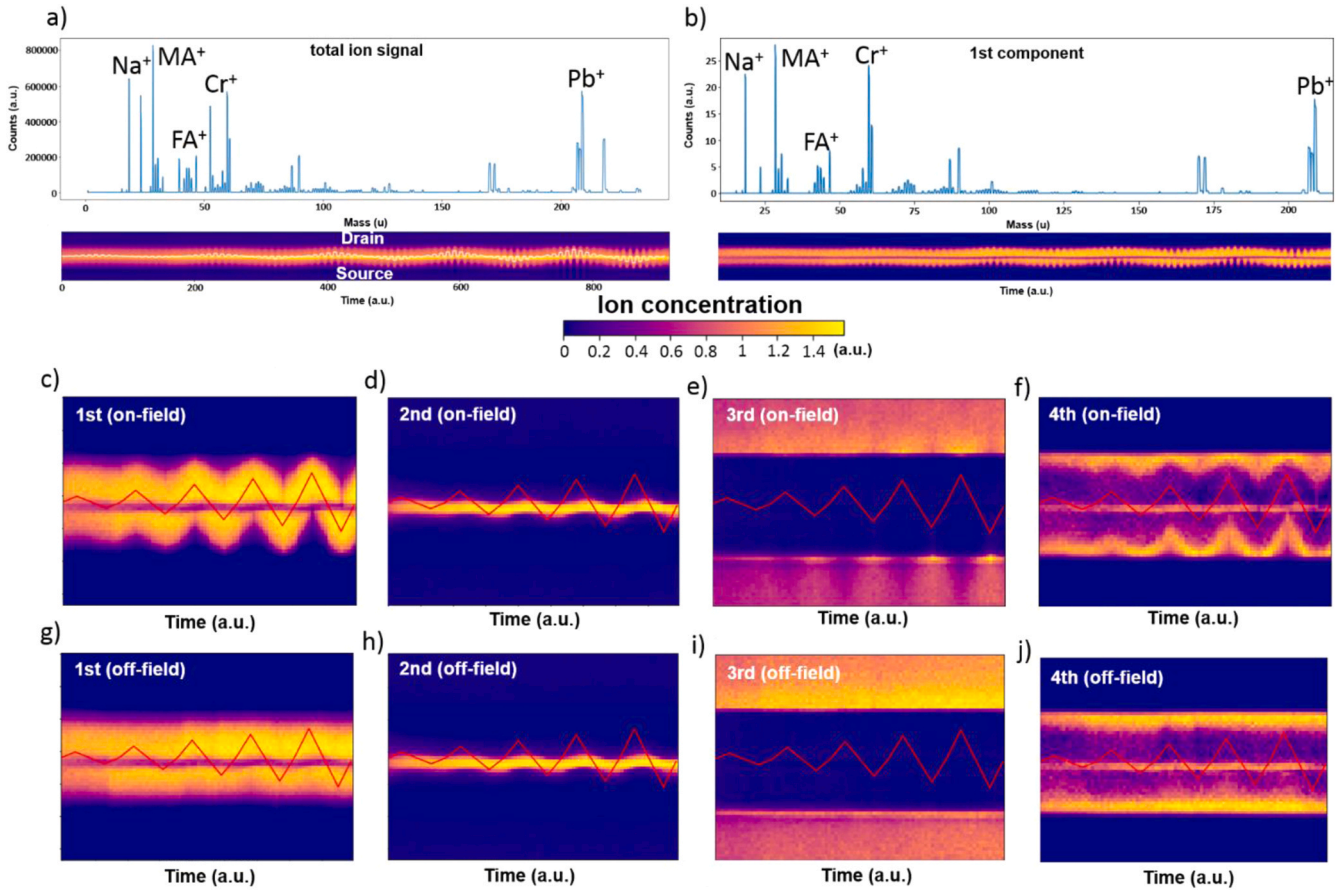

Fig. 4. The temporal evolution of positive ions in operando measured by tr-ToF-SIMS in the lateral perovskite device in dark condition. (a) The total mass spectra of positive ions (top) and the corresponding tr-ToF-SIMS map as a function of time and bias waveform (bottom). (b) The 1st NMF decomposition of tr-ToF-SIMS results (top) and the corresponding loading map as a function of time and bias (bottom). (c) The 1st, (d) 2nd, (e) 3rd, and (f) 4th NMF components of tr-ToF-SIMS maps in the on-field condition, and (g) the 1st, (h) 2nd, (i) 3rd, and (j) 4th NMF components in the off-field for positive ions in dark condition.

electrode regions. The MA^+ and Pb^+ ions are observed in the 4th NMF component (Fig. S20c), revealing a transient behavior, especially at the interface regions. Clearly, these identified ions can also contribute to the transient behavior in the *I-V* and CPD results, with dominant role of MA^+ ions in this phenomenon. This result is consistent with our previous study [40] on crucial role of mobile ions such as MA^+ and I^- ion in the *I-V* hysteresis in $MAPbI_3$ film. It was observed that both MA^+ and I^- ions have a similar effect under electric field in dark while MA^+ ions have a dominant effect than I^- ions under illumination [40]. Interestingly, a reduction of Pb^{2+} ions at the interface causes the depletion of Pb^{2+} at the bulk region due to the electrochemical reactions between Pb ions and Cr electrode. Again similar behavior was observed in lateral single crystal device [17]. Similar to the negative ToF-SIMS mode, the on- and off-field chemical maps are separately plotted in Fig. 4c–j. It is clearly seen that the ion migration occurs during the on-field condition (Fig. 4c–f) while the migrated ions are relaxed during the off-field condition (Fig. 4g–j). This is similar to the negative ion behavior. Particularly, positive ions including Na^+ ions during on-field migrate towards negatively charged electrodes. Overall, the result implies that positive ions such as FA^+, MA^+, Pb^{2+}, and Cr^+ migrate slower than negative ions in response to the electric waveform. Computational studies and experimental *I-V* measurements [90–92] suggested the slower migration of positive ions, here our result provides a direct visualization of slower migration of positive ions than halides.

The preponderant accumulation of Na^+ ions at the center region represents a highly unexpected finding in this work. We speculate that based on the preparation pathway and available data, the formation of this feature proceeded after the electrode deposition, and can be attributed to the surface transport away from the deposited electrodes with subsequently partial incorporation into MHP structure. This behavior is clearly suggested by the field response of the Na^+ ion feature that can be displaced by electric field but then relaxes to original position with time. Further studies will be done in the future to find this out.

Under illumination, positive ions are further explored, and the results are exhibited in Fig. S22. By comparing to the dark condition, less transient behavior is observed in the 1st, 2nd and 3rd NMF components which are almost similar. However, the 4th NMF component is relatively different, especially we see a significant reduction in the concentration of Pb^{2+} ions at the interfaces. The massive reduction of Pb^{2+} ions in the bulk region results from electrochemical reactions between Pb^+ ions and the injected charge carriers from the source electrode or the photogenerated charge carriers from perovskites in the vicinity of the electrode. We also separated the temporal changes of positive ions in the on- and off-field conditions under illumination (Fig. S23). We found that the migration of positive ions is also faster under illumination than dark condition and they are relaxed immediately in the off-fields. It is interesting to note that Cr^+ ions are stable in the 3rd NMF components (Fig. S23) which means that Cr^+ electrodes are not directly reacted with the perovskite layer especially at the interface under illumination and electric bias . However, it will be interesting to explore the long-term stability of perovskite in the vicinity of Cr electrode in the future studies.

Several studies suggested that *I-V* hysteresis in MHP devices is associated with various interfacial phenomena such as space charge layers, resulting from ion migration [93,94], interfacial charge accumulation and recombination [95], and charge trapping and de-trapping at the interface [96]. Particularly, ion migration has a critical role in the

hysteresis and transient phenomena in MHPs devices [9,90,96–101]. Ions are initially in the thermodynamically favored lattice sites but they can be migrated and redistributed under illumination and/or electric field. Using tr-ToF-SIMS technique, we analyzed the temporal evolution of ion dynamics and its role in the *I-V* and CPD hysteresis behavior. The results suggest that ion migration cannot significantly influence on the current and potential drop during the on-field condition except at the interfaces. Although ion migration across the device is directly observed in ToF-SIMS maps during the on-field conditions, the changes in *I-V* and CPD characteristics are relatively linear as a function of bias steps. However, it is important to note that ion migration results in accumulation of ions at the interface which has an impact on charge transport, interfacial defect passivation and even device stability. We found that the hysteresis behavior in the off-fields in both *I-V* and CPD measurements are due to the accumulation of charges at the interface. Using in operando ToF-SIMS measurements, we could further confirm the role of ions in the hysteresis phenomenon. Here, by combination of several techniques, we revealed the critical role of ion migration at the interfaces in transient behavior and hysteretic *I-V* and potential drop at the interfaces in MHP devices. We further demonstrated the role of charge injection and relaxation in the performance of mixed perovskite device in dark and under illumination. The time dependent ToF-SIMS characterization reveals that the most dominant mobile ions are halide ions such as I^- and Br^- in $(FAPbI_3)_{0.85}(MAPbBr_3)_{0.15}$ systems and particularly Br^- ions are accumulated at the interfaces. Nonetheless, the migration of organic cations cannot be ignored especially the MA^+ ions can be easily migrated between the biased electrodes. Besides, we found that Pb^{2+} ions can be reduced at the interfaces due to electrochemical reactions with the electrode in the presence of charge injection and photogenerated charge carriers. Our results clearly show the important role of interfacial phenomena and highlight that appropriate interface engineering will be an important key for highly efficient charge transport and stability in MHPs-based devices.

3. Conclusions

In summary, we have shown the role of ion migration in the lateral $Cr/(FAPbI_3)_{0.85}(MAPbBr_3)_{0.15}/Cr$ devices using a FORC bias waveform where the current, potential drop, and chemical changes can be characterized simultaneously in the on- and off-field conditions in dark and under illumination. The *I-V* characteristics of devices demonstrate a significant hysteretic behavior in the off-fields both in dark and under illumination while a transient behavior is more prominent in dark. The KPFM results reveal that the charge injection and relaxation with potential drops are significant at both interfaces than the bulk perovskite during on- and off-fields. Such dynamics are significantly reduced under illumination. From the analysis of chemical changes using tr-ToF-SIMS, the charge dynamics in *I-V* and CPD can be directly correlated with the ion migration and their interplay with electronic charges. Negative ions such as I^- and Br^- ions migrate in the on-fields and the migrated ions are relaxed in the off-fields in dark condition. We found that the migration of negative ions is faster under illumination. Particularly, Br^- ions highly accumulate at the interface between $(FAPbI_3)_{0.85}(MAPbBr_3)_{0.15}$ perovskite and drain electrode in both on- and off-fields, leading to hysteretic behaviors in the *I-V* and KPFM results. Positive ions such as FA^+ and MA^+ ions migrate and relax relatively slowly than negative ions both in dark and under illumination. Interestingly, MA^+ ions play an important role in transient behaviors due to their slow mobility. We found that under illumination Pb^{2+} ions are highly reduced at the interface due to electrochemical reactions with the electrode in the presence of charge injection and photogenerated charge carriers. While the ion migration can be fully or partially reversible, the electrochemical reaction at the interface can result in non-reversible phenomenon and induce permanent damage to the device performance and stability. Overall, the results reveal minor transient behavior and hysteresis in *I-V* and CPD distributions under illumination due to fast dynamics of photogenerated charges and ion migration. These results clearly show the significant role of interfacial phenomena and highlight that appropriate interface engineering is critical for highly efficient and stable MHPs-based devices. In addition, our study suggests that the MHPs-based devices with lower concentration of Br^- and MA^+ ions can have less hysteretic behaviors in mixed perovskites. Finally, this study provides insightful information regarding ion migration, electrochemical reaction, and associated charge dynamics in MHPs devices. This understanding is necessary to improving the stability of MHP devices and further inspire studies for investigation and control of hysteresis in these materials for application in memristors and energy storage devices.

4. Experimental section

Perovskite film synthesis: All the chemicals used here are purchased from Sigma-Aldrich and used without any further purifications. The $(FAPbI_3)_{0.85}(MAPbBr_3)_{0.15}$ precursor solution was prepared by dissolving 1.38 M of FAI and PbI_2, and 1.38 M of MABr and $PbBr_3$ in 0.8 ml N, N-dimethyl formamide (DMF, 99.9%) and 0.2 ml dimethyl sulfoxide (DMSO, 99.7%). The prepared $FAPbI_3$ and $MAPbBr_3$ precursor solutions are stirred at 60 ℃ for 1 h and then are mixed in proper ratio to form the $(FAPbI_3)_{0.85}(MAPbBr_3)_{0.15}$ precursor solution. The $(FAPbI_3)_{0.85}(MAPbBr_3)_{0.15}$ films were deposited on glass substrates ($15 \times 15 \times 1$ mm^3). The glass substrates (MSE Pro™) were precleaned using deionized water, acetone, and isopropanol in an ultrasonic bath for 15 min, respectively. After initial cleaning, the glass substrates were treated under UV ozone for 15 min. Then, the substrates are transferred into N_2-filled glove box. About 60 μL of the solution was dispersed onto the glass substrate and spin coated at 2000 rpm for 15 s following by 6000 rpm for 20 s where 150 μL of chlorobenzene was dropped during this stage. Finally, the samples were annealed at 100 ℃ for 10 min.

Fabrication of the devices: The 50 nm thick Cr electrodes were deposited by thermal evaporation using a shadow mask with a channel distance of around 70 μm between the lateral electrodes.

First order reversal curve (FORC) biases with on- and off-field on the lateral device: The FORC waveform electrical biases with on- and off-fields were applied to the lateral devices during I-V and KPFM measurements. The electrical biases were supplied by a Keithley 2450 source meter controlled by a test script builder. After applying biases in the dark, and then relaxation for 40 min in dark, photoelectric properties (e.g., photocurrent, photo-induced potential drop, and ion distribution) were measured under illumination with a white LED.

4.1. Characterizations and data analysis

Kelvin probe force microscopy (KPFM) measurements: KPFM measurements were carried out using an AFM (MFP-3D, Asylum Research) in a KPFM mode under ambient condition. The samples were measured immediately after they were transferred out of N_2-filled glove box. Consistent results have been achieved from repetitive measurements over 2 h in dark. KPFM measurements were performed using a Pt/Ir coated Si cantilever (ElectriMulti75-G, Budget Sensors) with lift height of 50 nm. During KPFM scans, FORC waveform was applied by an external function generator (Tektronix, Keithley 2450). A built-in white LED light source was used to illuminate the sample with a maximum intensity. In all KPFM measurements, the scan rate and size are 0.7 Hz on 512×512 pixels. The scan directions start from bottom to top, top to bottom, and bottom to top again during full FORC biases.

Time-resolved time-of-flight-secondary ion mass spectrometry (tr-ToF-SIMS) measurements: ToF-SIMS measurements were performed using ToF.SIMS5NCS instrument (IONTOF GmbH, Germany). Experiments were carried out in both negative and positive ion modes with spectra calibrated using the I-, Br-, CN-, CH-, Na+, MA+, FA+, Cr+, $CH_3(CH_2)_5^+$, $CH_3(CH_2)_7CH_3$+, $H_3N(CH_2)_{10}NH_3^+$, and Pb+ peaks. A built-in LED white light in ToF-SIMS chamber is used for illumination. The FORC biases were applied externally using a Tektronix AFG1022

arbitrary function generator (Tektronix, Beaverton, OR) and Lab View software.

Non-negative matrix factorization (NMF) analysis: NMF is a classical form of the unsupervised unmixing machine learning approach. This is an algorithm in multivariate analysis. An input data is factorized into desired endmember-abundance pairs with the property that all endmembers have no negative components. Particularly, this approach is suitable for analyzing ToF-SIMS data where all counting data is inherently non-negative due to calculating molecular mass. NMF data analysis was performed on google Colab using Python 3.6 and scikit-learn 0.19.2 library.

CRediT authorship contribution statement

Dohyung Kim: Conceptualization, Investigation, Validation, Resources, Data curation, Visualization, Writing – original draft. **Yongtao Liu**: Investigation, Software, Writing – review & draft. **Anton V. Ievlev**: Investigation, Data curation, Visualization, Writing – review & draft. **Kate Higgins**: Software, Writing – review & draft. **Olga S. Ovchinnikova**: Resources, Writing – review & draft. **Jae Sung Yun**: Investigation, Writing – review & draft. **Jan Seidel**: Resources, Writing – review & draft. **Sergei V. Kalinin**: Methodology, Conceptualization, Writing – review & draft. Mahshid Ahmadi: Conceptualization, Supervision, Project administration, Funding acquisition, Writing – review & draft.

Declaration of Competing Interest

The authors declare that they have no known competing financial interests or personal relationships that could have appeared to influence the work reported in this paper.

Acknowledgements

M.A. acknowledges support from the National Science Foundation (NSF), Award Number # 2043205. D.K., K.H., and M.A. acknowledge support from Center for Nanophase Materials Sciences (CNMS) which is a Departmnet of Energy (DOE) User Facility, project # CNMS2019-296 and CNMS2021-A-00706. K.H. was partially supported by the Center for Materials Processing (CMP), a Center of Excellence at the University of Tennessee, Knoxville funded by the Tennessee Higher Education Commission (THEC). The tr-ToF-SIMS measurements were conducted and supported (A.V. I., O. S. O., S.V.K., Y.L.) at the Center for Nanophase Materials Sciences (CNMS).

Appendix A. Supporting information

Supplementary data associated with this article can be found in the online version at doi:10.1016/j.nanoen.2021.106428.

References

[1] ⟨https://www.nrel.gov/pv/cell-efficiency.html⟩. Access on 04 January 2021.
[2] Z. Xiao, R.A. Kerner, L. Zhao, N.L. Tran, K.M. Lee, T.-W. Koh, G.D. Scholes, B. P. Rand, Efficient perovskite light-emitting diodes featuring nanometre-sized crystallites, Nat. Photonics 11 (2017) 108–115.
[3] M. Ahmadi, T. Wu, B. Hu, A review on organic–inorganic halide perovskite photodetectors: device engineering and fundamental physics, Adv. Mater. 29 (2017), 1605242.
[4] H. Wei, J. Huang, Halide lead perovskites for ionizing radiation detection, Nat. Commun. 10 (2019) 1066.
[5] J. Choi, S. Park, J. Lee, K. Hong, D.-H. Kim, C.W. Moon, G.D. Park, J. Suh, J. Hwang, S.Y. Kim, H.S. Jung, N.-G. Park, S. Han, K.T. Nam, H.W. Jang, Organolead halide perovskites for low operating voltage multilevel resistive switching, Adv. Mater. 28 (2016) 6562–6567.
[6] E.J. Juarez-Perez, R.S. Sanchez, L. Badia, G. Garcia-Belmonte, Y.S. Kang, I. Mora-Sero, J. Bisquert, Photoinduced giant dielectric constant in lead halide perovskite solar cells, J. Phys. Chem. Lett. 5 (2014) 2390–2394.
[7] E.T. Hoke, D.J. Slotcavage, E.R. Dohner, A.R. Bowring, H.I. Karunadasa, M. D. McGehee, Reversible photo-induced trap formation in mixed-halide hybrid perovskites for photovoltaics, Chem. Sci. 6 (2015) 613–617.
[8] H. Tsai, R. Asadpour, J.-C. Blancon, C.C. Stoumpos, O. Durand, J.W. Strzalka, B. Chen, R. Verduzco, P.M. Ajayan, S. Tretiak, J. Even, M.A. Alam, M. G. Kanatzidis, W. Nie, A.D. Mohite, Light-induced lattice expansion leads to high-efficiency perovskite solar cells, Science 360 (2018) 67–70.
[9] Y. Yuan, J. Chae, Y. Shao, Q. Wang, Z. Xiao, A. Centrone, J. Huang, Photovoltaic switching mechanism in lateral structure hybrid perovskite solar cells, Adv. Energy Mater. 5 (2015), 1500615.
[10] Y. Yuan, T. Li, Q. Wang, J. Xing, A. Gruverman, J. Huang, Anomalous photovoltaic effect in organic-inorganic hybrid perovskite solar cells, Sci. Adv. 3 (2017), 1602164.
[11] D. Kim, J.S. Yun, P. Sharma, D.S. Lee, J. Kim, A.M. Soufiani, S. Huang, M. A. Green, A.W.Y. Ho-Baillie, J. Seidel, Light- and bias-induced structural variations in metal halide perovskites, Nat. Commun. 10 (1) (2019), https://doi.org/10.1038/s41467-019-08364-1, 444.
[12] J.M. Azpiroz, E. Mosconi, J. Bisquert, F. De, Defect migration in methylammonium lead iodide and its role in perovskite solar cell operation, Energy Environ. Sci. 8 (2015) 2118–2127.
[13] J. Haruyama, K. Sodeyama, L. Han, Y. Tateyama, First-principles study of ion diffusion in perovskite solar cell sensitizers, J. Am. Chem. Soc. 137 (2015) 10048–10051.
[14] C. Li, A. Guerrero, Y. Zhong, S. Huettner, Origins and mechanisms of hysteresis in organometal halide perovskites, J. Phys. Condens. Matter Inst. Phys. J. 29 (2017), 193001.
[15] H. Yu, H. Lu, F. Xie, S. Zhou, N. Zhao, Native defect-induced hysteresis behavior in organolead iodide perovskite solar cells, Adv. Funct. Mater. 26 (2016) 1411–1419.
[16] C. Zhao, B. Chen, X. Qiao, L. Luan, K. Lu, B. Hu, Revealing underlying processes involved in light soaking effects and hysteresis phenomena in perovskite solar cells, Adv. Energy Mater. 5 (2015), 1500279.
[17] K. Higgins, M. Lorenz, M. Ziatdinov, R.K. Vasudevan, A.V. Ievlev, E.D. Lukosi, O. S. Ovchinnikova, S.V. Kalinin, M. Ahmadi, Exploration of electrochemical reactions at organic–inorganic halide perovskite interfaces via machine learning in in situ time-of-flight secondary ion mass spectrometry, Adv. Funct. Mater. 30 (2020), 2001995.
[18] K. Domanski, J.-P. Correa-Baena, N. Mine, M.K. Nazeeruddin, A. Abate, M. Saliba, W. Tress, A. Hagfeldt, M. Grätzel, Not all that glitters is gold: metal-migration-induced degradation in perovskite solar cells, ACS Nano 10 (2016) 6306–6314.
[19] C.C. Boyd, R. Cheacharoen, K.A. Bush, R. Prasanna, T. Leijtens, M.D. McGehee, Barrier design to prevent metal-induced degradation and improve thermal stability in perovskite solar cells, ACS Energy Lett. 3 (2018) 1772–1778.
[20] T. Zhang, X. Meng, Y. Bai, S. Xiao, C. Hu, Y. Yang, H. Chen, S. Yang, Profiling the organic cation-dependent degradation of organolead halide perovskite solar cells, J. Mater. Chem. A 5 (2017) 1103–1111.
[21] M. Lira-Cantú, Perovskite solar cells: stability lies at interfaces, Nat. Energy 2 (2017) 17115.
[22] P. Schulz, D. Cahen, A. Kahn, Halide perovskites: is it all about the interfaces? Chem. Rev. 119 (2019) 3349–3417.
[23] S. Guarnera, A. Abate, W. Zhang, J.M. Foster, G. Richardson, A. Petrozza, H. J. Snaith, J. Phys. Chem. Lett. 6 (2015) 432–437.
[24] V. Babu, R. Fuentes Pineda, T. Ahmad, A.O. Alvarez, L.A. Castriotta, A. Di Carlo, F. Fabregat-Santiago, K. Wojciechowski, Improved stability of inverted and flexible perovskite solar cells with carbon electrode, ACS Appl. Energy Mater. 3 (2020) 5126–5134.
[25] M. Kaltenbrunner, G. Adam, E.D. Głowacki, M. Drack, R. Schwödiauer, L. Leonat, D.H. Apaydin, H. Groiss, M.C. Scharber, M.S. White, N.S. Sariciftci, S. Bauer, Flexible high power-per-weight perovskite solar cells with chromium oxide-metal contacts for improved stability in air, Nat. Mater. 14 (2015) 1032–1039.
[26] J.T. Tisdale, E. Muckley, M. Ahmadi, T. Smith, C. Seal, E. Lukosi, I.N. Ivanov, B. Hu, Dynamic impact of electrode materials on interface of single-crystalline methylammonium lead bromide perovskite, Adv. Mater. Interfaces 5 (2018), 1800476.
[27] ormation and diffusion of metal impurities in perovskite solar cell material CH3NH3PbI3: implications on solar cell degradation and choice W. Ming, D. Yang, T. Li, L. Zhang, M.-H. Du, Formation and diffusion of metal impurities in perovskite solar cell material $CH_3NH_3PbI_3$: implications on solar cell degradation and choice of electrode, Adv. Sci. 5 (2018), 1700662.
[28] F. Behrouznejad, S. Shahbazi, N. Taghavinia, H.-P. Wu, E. Wei-Guang, A study on utilizing different metals as the back contact of $CH_3NH_3PbI_3$ perovskite solar cells, J. Mater. Chem. A 4 (2016) 13488–13498.
[29] J. Zhao, X. Zheng, Y. Deng, T. Li, Y. Shao, A. Gruverman, J. Shield, J. Huang, Is Cu a stable electrode material in hybrid perovskite solar cells for a 30-year lifetime, Energy Environ. Sci. 9 (2016) 3650–3656.
[30] Y. Liu, A.V. Ievlev, L. Collins, A. Belianinov, J.K. Keum, M. Ahmadi, S. Jesse, S. T. Retterer, K. Xiao, J. Huang, B.G. Sumpter, S.V. Kalinin, B. Hu, O. S. Ovchinnikova, Strain–chemical gradient and polarization in metal halide perovskites, Adv. Electron. Mater. 6 (2020), 1901235.
[31] L. Collins, M. Ahmadi, J. Qin, Y. Liu, O.S. Ovchinnikova, B. Hu, S. Jesse, S. V. Kalinin, Time resolved surface photovoltage measurements using a big data capture approach to KPFM, Nanotechnology 29 (2018), 445703.
[32] J.L. Garrett, E.M. Tennyson, M. Hu, J. Huang, J.N. Munday, M.S. Leite, Real-time nanoscale open-circuit voltage dynamics of perovskite solar cells, Nano Lett. 17 (2017) 2554–2560.
[33] R. Giridharagopal, J.T. Precht, S. Jariwala, L. Collins, S. Jesse, S.V. Kalinin, D. S. Ginger, Time-resolved electrical scanning probe microscopy of layered perovskites reveals spatial variations in photoinduced ionic and electronic carrier motion, ACS Nano 13 (2019) 2812–2821.

[34] V.W. Bergmann, Y. Guo, H. Tanaka, I.M. Hermes, D. Li, A. Klasen, S. A. Bretschneider, E. Nakamura, R. Berger, S.A.L. Weber, Local time-dependent charging in a perovskite solar cell, ACS Appl. Mater. Interfaces 8 (2016) 19402–19409.

[35] L. Collins, A. Belianinov, S. Somnath, N. Balke, S.V. Kalinin, S. Jesse, Full data acquisition in Kelvin Probe Force Microscopy: mapping dynamic electric phenomena in real space, Sci. Rep. 6 (2016) 30557.

[36] L. Collins, A. Belianinov, S. Somnath, B.J. Rodriguez, N. Balke, S.V. Kalinin, S. Jesse, Multifrequency spectrum analysis using fully digital G Mode-Kelvin probe force microscopy, Nanotechnology 27 (2016), 105706.

[37] L. Collins, M. Ahmadi, T. Wu, B. Hu, S.V. Kalinin, S. Jesse, Breaking the time barrier in Kelvin probe force microscopy: fast free force reconstruction using the G-mode platform, ACS Nano 11 (2017) 8717–8729.

[38] E. Strelcov, S. Jesse, Y.-L. Huang, Y.-C. Teng, I.I. Kravchenko, Y.-H. Chu, S. V. Kalinin, Space- and time-resolved mapping of ionic dynamic and electroresistive phenomena in lateral devices, ACS Nano 7 (2013) 6806–6815.

[39] W. Melitz, J. Shen, A.C. Kummel, S. Lee, Kelvin probe force microscopy and its application, Surf. Sci. Rep. 66 (2011) 1–27.

[40] Y. Liu, N. Borodinov, M. Lorenz, M. Ahmadi, S.V. Kalinin, A.V. Ievlev, O. S. Ovchinnikova, Hysteretic ion migration and remanent field in metal halide perovskites, Adv. Sci. 7 (2020), 2001176.

[41] Y. Liu, A.V. Ievlev, N. Borodinov, M. Lorenz, K. Xiao, M. Ahmadi, B. Hu, S. V. Kalinin, O.S. Ovchinnikova, Direct observation of photoinduced ion migration in lead halide perovskites, Adv. Funct. Mater. 31 (2020), 2008777.

[42] N.J. Jeon, J.H. Noh, W.S. Yang, Y.C. Kim, S. Ryu, J. Seo, S.I. Seok, Compositional engineering of perovskite materials for high-performance solar cells, Nature 517 (2015) 476–480.

[43] W.S. Yang, J.H. Noh, N.J. Jeon, Y.C. Kim, S. Ryu, J. Seo, S.I. Seok, High-performance photovoltaic perovskite layers fabricated through intramolecular exchange, Science 348 (2015) 1234–1237.

[44] N.J. Jeon, J.H. Noh, Y.C. Kim, W.S. Yang, S. Ryu, S.I. Seok, Solvent engineering for high-performance inorganic-organic hybrid perovskite solar cells, Nat. Mater. 13 (2014) 897–903.

[45] E.H. Jung, N.J. Jeon, E.Y. Park, C.S. Moon, T.J. Shin, T.-Y. Yang, J.H. Noh, J. Seo, Efficient, stable and scalable perovskite solar cells using poly(3-hexylthiophene), Nature 567 (2019) 511–515.

[46] Y. Wang, T. Mahmoudi, Y.-B. Hahn, Highly stable and efficient perovskite solar cells based on FAMA-perovskite-Cu:NiO composites with 20.7% efficiency and 80.5% fill factor, Adv. Energy Mater. 10 (2020), 2000967.

[47] S. You, X. Xi, X. Zhang, H. Wang, P. Gao, X. Ma, S. Bi, J. Zhang, H. Zhou, Z. Wei, Long-term stable and highly efficient perovskite solar cells with a formamidinium chloride (FACl) additive, J. Mater. Chem. A 8 (2020) 17756–17764.

[48] A.R. Muxworthy, A.P. Roberts, Springer Netherlands, Dordrecht, 2007, pp. 266–272.

[49] Y. Kim, A. Kumar, O. Ovchinnikov, S. Jesse, H. Han, D. Pantel, I. Vrejoiu, W. Lee, D. Hesse, M. Alexe, S.V. Kalinin, First-order reversal curve probing of spatially resolved polarization switching dynamics in ferroelectric nanocapacitors, ACS Nano 6 (2012) 491–500.

[50] S.M. Yang, E. Strelcov, M.P. Paranthaman, A. Tselev, T.W. Noh, S.V. Kalinin, Humidity effect on nanoscale electrochemistry in solid silver ion conductors and the dual nature of its locality, Nano Lett. 15 (2015) 1062–1069.

[51] E. Strelcov, A. Belianinov, Y.H. Hsieh, S. Jesse, A.P. Baddorf, Y.H. Chu, S. V. Kalinin, Deep data analysis of conductive phenomena on complex oxide interfaces: physics from data mining, ACS Nano 8 (2014) 6449–6457.

[52] E. Strelcov, Y. Kim, S. Jesse, Y. Cao, I.N. Ivanov, I.I. Kravchenko, C.H. Wang, Y. C. Teng, L.Q. Chen, Y.H. Chu, S.V. Kalinin, Probing local ionic dynamics in functional oxides at the nanoscale, Nano Lett. 13 (2013) 3455–3462.

[53] N. Balke, S. Jesse, Y. Kim, L. Adamczyk, I.N. Ivanov, N.J. Dudney, S.V. Kalinin, Decoupling electrochemical reaction and diffusion processes in ionically-conductive solids on the nanometer scale, ACS Nano 4 (2010) 7349–7357.

[54] S. Guo, O.S. Ovchinnikov, M.E. Curtis, M.B. Johnson, S. Jesse, S.V. Kalinin, Spatially resolved probing of Preisach density in polycrystalline ferroelectric thin films, J. Appl. Phys. 108 (2010), 084103.

[55] K. Seal, S. Jesse, M.P. Nikiforov, S.V. Kalinin, I. Fujii, P. Bintachitt, S. Trolier-McKinstry, Spatially resolved spectroscopic mapping of polarization reversal in polycrystalline ferroelectric films: crossing the resolution barrier, Phys. Rev. Lett. 103 (2009), 057601.

[56] Y. Kim, E. Strelcov, I.R. Hwang, T. Choi, B.H. Park, S. Jesse, S.V. Kalinin, Correlative multimodal probing of ionically-mediated electromechanical phenomena in simple oxides, Sci. Rep. 3 (2013) 2924.

[57] D.S. Lee, J.S. Yun, J. Kim, A.M. Soufiani, S. Chen, Y. Cho, X. Deng, J. Seidel, S. Lim, S. Huang, A.W.Y. Ho-Baillie, Passivation of Grain Boundaries by Phenethylammonium in Formamidinium-Methylammonium Lead Halide Perovskite Solar Cells, ACS Energy Lett. 3 (3) (2018) 647–654.

[58] A. Kumar, Y. Ehara, A. Wada, H. Funakubo, F. Griggio, S. Trolier-McKinstry, S. Jesse, S.V. Kalinin, Dynamic piezoresponse force microscopy: spatially resolved probing of polarization dynamics in time and voltage domains, J. Appl. Phys. 112 (2012), 052021.

[59] J.S. Yun, J. Kim, T. Young, R.J. Patterson, D. Kim, J. Seidel, S. Lim, M.A. Green, S. Huang, A. Ho-Baillie, Humidity-induced degradation via grain boundaries of $HC(NH_2)_2PbI_3$ Planar perovskite solar cells, Adv. Funct. Mater. 28 (2018), 1705363.

[60] S. Jesse, B.J. Rodriguez, S. Choudhury, A.P. Baddorf, I. Vrejoiu, D. Hesse, M. Alexe, E.A. Eliseev, A.N. Morozovska, J. Zhang, L.-Q. Chen, S.V. Kalinin, Direct imaging of the spatial and energy distribution of nucleation centres in ferroelectric materials, Nat. Mater. 7 (2008) 209–215.

[61] B. Chen, M. Yang, X. Zheng, C. Wu, W. Li, Y. Yan, J. Bisquert, G. Garcia-Belmonte, K. Zhu, S. Priya, Impact of capacitive effect and ion migration on the hysteretic behavior of perovskite solar cells, J. Phys. Chem. Lett. 6 (2015) 4693–4700.

[62] P. Li, Y. Zhang, C. Liang, G. Xing, X. Liu, F. Li, X. Liu, X. Hu, G. Shao, Y. Song, Phase pure 2D perovskite for high-performance 2D–3D heterostructured perovskite solar cells, Adv. Mater. 30 (2018), 1805323.

[63] G.H. Enevoldsen, T. Glatzel, M.C. Christensen, J.V. Lauritsen, F. Besenbacher, Atomic scale Kelvin probe force microscopy studies of the surface potential variations on the TiO2(110) surface, Phys. Rev. Lett. 100 (2008), 236104.

[64] A. Pockett, G.E. Eperon, T. Peltola, H.J. Snaith, A. Walker, L.M. Peter, P. J. Cameron, Characterization of planar lead halide perovskite solar cells by impedance spectroscopy, open-circuit photovoltage decay, and intensity-modulated photovoltage/photocurrent spectroscopy, J. Phys. Chem. C 119 (2015) 3456–3465.

[65] A.R. Pascoe, N.W. Duffy, A.D. Scully, F. Huang, Y.-B. Cheng, Insights into planar $CH_3NH_3PbI_3$ Perovskite solar cells using impedance spectroscopy, J. Phys. Chem. C 119 (2015) 4444–4453.

[66] I. Zarazua, G. Han, P.P. Boix, S. Mhaisalkar, F. Fabregat-Santiago, I. Mora-Seró, J. Bisquert, G. Garcia-Belmonte, Surface recombination and collection efficiency in perovskite solar cells from impedance analysis, J. Phys. Chem. Lett. 7 (2016) 5105–5113.

[67] S. van Reenen, M. Kemerink, H.J. Snaith, Modeling anomalous hysteresis in perovskite solar cells, J. Phys. Chem. Lett. 6 (2015) 3808–3814.

[68] D.A. Jacobs, Y. Wu, H. Shen, C. Barugkin, F.J. Beck, T.P. White, K. Weber, K. R. Catchpole, Hysteresis phenomena in perovskite solar cells: the many and varied effects of ionic accumulation, Phys. Chem. Chem. Phys. 19 (2017) 3094–3103.

[69] E. Strelcov, A.V. Ievlev, S. Jesse, I.I. Kravchenko, V.Y. Shur, S.V. Kalinin, Direct probing of charge injection and polarization-controlled ionic mobility on ferroelectric $LiNbO_3$ surfaces, Adv. Mater. 26 (2014) 958–963.

[70] Y. Zhao, P. Miao, J. Elia, H. Hu, X. Wang, T. Heumueller, Y. Hou, G.J. Matt, A. Osvet, Y.-T. Chen, M. Tarragó, D. de Ligny, T. Przybilla, P. Denninger, J. Will, J. Zhang, X. Tang, N. Li, C. He, A. Pan, A.J. Meixner, E. Spiecker, D. Zhang, C. J. Brabec, Strain-activated light-induced halide segregation in mixed-halide perovskite solids, Nat. Commun. 11 (2020) 6328.

[71] A.J. Knight, J. Borchert, R.D.J. Oliver, J.B. Patel, P.G. Radaelli, H.J. Snaith, M. B. Johnston, L.M. Herz, Halide segregation in mixed-halide perovskites: influence of A-site cations, ACS Energy Lett. 6 (2021) 799–808.

[72] S.J. Yoon, S. Draguta, J.S. Manser, O. Sharia, W.F. Schneider, M. Kuno, P. V. Kamat, Tracking iodide and bromide ion segregation in mixed halide lead perovskites during photoirradiation, ACS Energy Lett. 1 (2016) 290–296.

[73] A.J. Knight, A.D. Wright, J.B. Patel, D.P. McMeekin, H.J. Snaith, M.B. Johnston, L.M. Herz, Electronic traps and phase segregation in lead mixed-halide perovskite, ACS Energy Lett. 4 (2019) 75–84.

[74] R.M. Kennard, C.J. Dahlman, H. Nakayama, R.A. DeCrescent, J.A. Schuller, R. Seshadri, K. Mukherjee, M.L. Chabinyc, Phase stability and diffusion in lateral heterostructures of methyl ammonium lead halide perovskites, ACS Appl. Mater. Interfaces 11 (2019) 25313–25321.

[75] S.J. Yoon, M. Kuno, P.V. Kamat, Shift happens. How halide ion defects influence photoinduced segregation in mixed halide perovskites, ACS Energy Lett. 2 (2017) 1507–1514.

[76] C. Zhu, X. Niu, Y. Fu, N. Li, C. Hu, Y. Chen, X. He, G. Na, P. Liu, H. Zai, Y. Ge, Y. Lu, X. Ke, Y. Bai, S. Yang, P. Chen, Y. Li, M. Sui, L. Zhang, H. Zhou, Q. Chen, Strain engineering in perovskite solar cells and its impacts on carrier dynamics, Nat. Commun. 10 (2019) 815.

[77] J. Kim, J.S. Yun, Y. Cho, D.S. Lee, B. Wilkinson, A.M. Soufiani, X. Deng, J. Zheng, A. Shi, S. Lim, S. Chen, Z. Hameiri, M. Zhang, C.F.J. Lau, S. Huang, M.A. Green, A. W.Y. Ho-Baillie, Overcoming the challenges of large-area high-efficiency perovskite solar cells, ACS Energy Lett. 2 (2017) 1978–1984.

[78] A.J. Barker, A. Sadhanala, F. Deschler, M. Gandini, S.P. Senanayak, P.M. Pearce, E. Mosconi, A.J. Pearson, Y. Wu, A.R. Srimath Kandada, T. Leijtens, F. De Angelis, S.E. Dutton, A. Petrozza, R.H. Friend, Defect-assisted photoinduced halide segregation in mixed-halide perovskite thin films, ACS Energy Lett. 2 (2017) 1416–1424.

[79] F. Wang, S. Bai, W. Tress, A. Hagfeldt, F. Gao, Defects engineering for high-performance perovskite solar cells, npj Flex. Electron. 2 (2018) 22.

[80] D. Meggiolaro, E. Mosconi, F. De Angelis, Formation of surface defects dominates ion migration in lead-halide perovskites, ACS Energy Lett. 4 (2019) 779–785.

[81] D.W. de Quilettes, S.M. Vorpahl, S.D. Stranks, H. Nagaoka, G.E. Eperon, M. E. Ziffer, H.J. Snaith, D.S. Ginger, Impact of microstructure on local carrier lifetime in perovskite solar cells, Science 348 (2015) 683–686.

[82] T.A.S. Doherty, A.J. Winchester, S. Macpherson, D.N. Johnstone, V. Pareek, E. M. Tennyson, S. Kosar, F.U. Kosasih, M. Anaya, M. Abdi-Jalebi, Z. Andaji-Garmaroudi, E.L. Wong, J. Madéo, Y.-H. Chiang, J.-S. Park, Y.-K. Jung, C. E. Petoukhoff, G. Divitini, M.K.L. Man, C. Ducati, A. Walsh, P.A. Midgley, K. M. Dani, S.D. Stranks, Performance-limiting nanoscale trap clusters at grain junctions in halide perovskites, Nature 580 (2020) 360–366.

[83] Y.-C. Zhao, W.-K. Zhou, X. Zhou, K.-H. Liu, D.-P. Yu, Q. Zhao, Light Sci. Appl. 6 (2017) e16243-e16243.

[84] J. Xing, Q. Wang, Q. Dong, Y. Yuan, Y. Fang, J. Huang, Ultrafast ion migration in hybrid perovskite polycrystalline thin films under light and suppression in single crystals, Phys. Chem. Chem. Phys. 18 (2016) 30484–30490.

[85] Z. Andaji-Garmaroudi, M. Abdi-Jalebi, F.U. Kosasih, T. Doherty, S. Macpherson, A.R. Bowman, G.J. Man, U.B. Cappel, H. Rensmo, C. Ducati, R.H. Friend, S. D. Stranks, Elucidating and mitigating degradation processes in perovskite light-emitting diodes, Adv. Energy Mater. 10 (2020), 2002676.

[86] Y. Zhou, F. Wang, H.-H. Fang, M.A. Loi, F.-Y. Xie, N. Zhao, C.-P. Wong, Distribution of bromine in mixed iodide–bromide organolead perovskites and its impact on photovoltaic performance, J. Mater. Chem. A 4 (2016) 16191–16197.
[87] C. Bi, X. Zheng, B. Chen, H. Wei, J. Huang, Spontaneous passivation of hybrid perovskite by sodium ions from glass substrates: mysterious enhancement of device efficiency revealed, ACS Energy Lett. 2 (2017) 1400–1406.
[88] N. Ueoka, T. Oku, Effects of co-addition of sodium chloride and copper(II) bromide to mixed-cation mixed-halide perovskite photovoltaic devices, ACS Appl. Energy Mater. 3 (2020) 7272–7283.
[89] S.P. Harvey, J.A. Aguiar, P. Hacke, H. Guthrey, S. Johnston, M. Al-Jassim, Sodium accumulation at potential-induced degradation shunted areas in polycrystalline silicon modules, IEEE J. Photovolt. 6 (2016) 1440–1445.
[90] C. Eames, J.M. Frost, P.R.F. Barnes, B.C. O'Regan, A. Walsh, M.S. Islam, Ionic transport in hybrid lead iodide perovskite solar cells, Nat. Commun. 6 (2015) 7497.
[91] X. Zhu, J. Lee, W.D. Lu, Iodine vacancy redistribution in organic–inorganic halide perovskite films and resistive switching effects, Adv. Mater. 29 (2017), 1700527.
[92] W.-J. Yin, T. Shi, Y. Yan, Unusual defect physics in $CH_3NH_3PbI_3$ perovskite solar cell absorber, Appl. Phys. Lett. 104 (2014), 063903.
[93] E. Mosconi, F. De Angelis, Mobile ions in organohalide perovskites: interplay of electronic structure and dynamics, ACS Energy Lett. 1 (2016) 182–188.
[94] W. Tress, Metal halide perovskites as mixed electronic-ionic conductors: challenges and opportunities-from hysteresis to memristivity, J. Phys. Chem. Lett. 8 (2017) 3106–3114.
[95] Y. Rong, Y. Hu, S. Ravishankar, H. Liu, X. Hou, Y. Sheng, A. Mei, Q. Wang, D. Li, M. Xu, J. Bisquert, H. Han, Tunable hysteresis effect for perovskite solar cells, Energy Environ. Sci. 10 (2017) 2383–2391.
[96] H.J. Snaith, A. Abate, J.M. Ball, G.E. Eperon, T. Leijtens, N.K. Noel, S.D. Stranks, J.T.-W. Wang, K. Wojciechowski, W. Zhang, Anomalous hysteresis in perovskite solar cells, J. Phys. Chem. Lett. 5 (2014) 1511–1515.
[97] W. Tress, N. Marinova, T. Moehl, S.M. Zakeeruddin, M.K. Nazeeruddin, M. Grätzel, Understanding the rate-dependent *J–V* hysteresis, slow time component, and aging in $CH_3NH_3PbI_3$ perovskite solar cells: the role of a compensated electric field, Energy Environ. Sci. 8 (2015) 995–1004.
[98] E.L. Unger, E.T. Hoke, C.D. Bailie, W.H. Nguyen, A.R. Bowring, T. Heumüller, M. G. Christoforo, M.D. McGehee, Hysteresis and transient behavior in current–voltage measurements of hybrid-perovskite absorber solar cells, Energy Environ. Sci. 7 (2014) 3690–3698.
[99] G.E. Eperon, G.M. Paternò, R.J. Sutton, A. Zampetti, A.A. Haghighirad, F. Cacialli, H.J. Snaith, Inorganic caesium lead iodide perovskite solar cells, J. Mater. Chem. A 3 (2015) 19688–19695.
[100] Z. Xiao, Y. Yuan, Y. Shao, Q. Wang, Q. Dong, C. Bi, P. Sharma, A. Gruverman, J. Huang, Giant switchable photovoltaic effect in organometal trihalide perovskite devices, Nat. Mater. 14 (2015) 193–198.
[101] Y. Shao, Z. Xiao, C. Bi, Y. Yuan, J. Huang, Origin and elimination of photocurrent hysteresis by fullerene passivation in $CH_3NH_3PbI_3$ planar heterojunction solar cells, Nat. Commun. 5 (2014) 5784.
[102] D. Kim, E.S. Muckley, N. Creange, T.H. Wan, M.H. Ann, E. Quattrocchi, R. K. Vasudevan, J.H. Kim, F. Ciucci, I.N. Ivanov, S.V. Kalinin, M. Ahmadi, Exploring Transport Behavior in Hybrid Perovskites Solar Cells via Machine Learning Analysis of Environmental-Dependent Impedance Spectroscopy, Advanced Science 8 (15) (2021), 2002510, https://doi.org/10.1002/advs.202002510.